

Adsorption and mechanism of nitrate from groundwater onto Si–Al porous clay mineral material as ceramic waste: characterization, kinetics, and adsorption isotherms

Liping Jia^{a,b}, Binhui Jiang^b, Fei Huang^b, Xiaomin Hu^{b,*}

^aCollege of Chemistry, Chemical Engineering and Environment, Minnan Normal University, Zhangzhou 363000, China, Tel. +86-13342480321; email: lipingjia@stumail.neu.edu.cn (L. Jia)

^bCollege of Resource and Civil Engineering, Northeastern University, Shenyang 110819, China, Tel. +86-13940307916; email: hxmin_jj@163.com (X. Hu), Tel. +86-1332445601; email: jiangbinhui@mail.neu.edu.cn (B. Jiang), Tel. 86-13322402458; email: huangfei@mail.neu.edu.cn (F. Huang)

Received 15 October 2019; Accepted 1 June 2020

ABSTRACT

A Si–Al porous clay mineral material W (PCMW) as raw material for ceramic was prepared from two kinds of natural clay minerals. The waste of PCMW could be used as an adsorbent to remove nitrate ($\text{NO}_3\text{-N}$) from groundwater. The characteristics of PCMW were determined by surface area, pore volume, scanning electron microscopy, X-ray fluorescence, powder X-ray diffraction, $\text{pH}_{\text{(zpc)}}$, Fourier transform infrared spectroscopy, and zeta potential analyses. The optimum values of the effective parameters, such as the contact time (96–120 h), pH (<6.0), initial concentrations of $\text{NO}_3\text{-N}$ (25–40 mg/L), PCMW dosage (0.5–2 g), particle size of PCMW (1–3 mm), and temperature (288–303 K), were determined. The pseudo-first-order kinetic model and the Langmuir isotherm effectively described the adsorption process; the maximum adsorption capacity of PCMW as calculated from this model was 5.14–5.30 mg/g. Intraparticle diffusion and liquid film diffusion could affect the adsorption process. Kinetic models, isotherm models, and thermodynamic calculations demonstrated that the adsorption of $\text{NO}_3\text{-N}$ onto PCMW was a kinetically controlled, spontaneous, and endothermic monolayer physical process. The results of this study suggest that PCMW is suitable as a recyclable adsorbent material for the adsorption of $\text{NO}_3\text{-N}$ from groundwater.

Keywords: Si–Al clay mineral porous material; Groundwater; Nitrate; Waste reuse; Adsorption kinetics; Adsorption isotherms

1. Introduction

Unreasonable disposal of industrial wastewater and sewage, the presence of garbage and excrement, and the excessive application of chemical fertilizers have caused widespread nitrate ($\text{NO}_3\text{-N}$) contamination of groundwater to varying degrees [1–4]. In China, 37% of groundwater was met the Class V specifications of the quality standard for groundwater (GB/T 14848–93), which seriously threatens the environmental safety of groundwater drinking water sources and increases environmental risks [5]. Although $\text{NO}_3\text{-N}$ is a relatively nontoxic substance, excessive amounts

of $\text{NO}_3\text{-N}$ in groundwater can harm human health through organ damage, liver damage, and methemoglobinemia and even can trigger cancer via long-term intake of an overdose of $\text{NO}_3\text{-N}$ [6–8].

The common methods to remove $\text{NO}_3\text{-N}$ from groundwater are permeable reactive barrier (PRB) [9,10], membrane separation technique [11,12], biological [13,14], electrochemical [15,16], and adsorption [17,18]. All these methods have limitations, such as producing toxic byproducts and secondary waste, especially nitrite [19–21], which require continuous monitoring of the growth of microorganisms and a constant supply of energy or organic substrates [22–24].

* Corresponding author.

In practical applications, the adsorption method seems to be one of the most favored wastewater treatment techniques due to its low cost, easy operation, strong practicability, and high efficiency.

The adsorption materials used to remove $\text{NO}_3\text{-N}$ included modified attapulgite [6], ion exchange resin [25], modified activated carbon [26], zeolite [27,28], clay [29–31], etc. Natural clay minerals in their pristine form can act as adsorbents, which are inexpensive, have a large surface area, exhibit swelling, participate in ion exchange in aqueous systems, and have no toxic effects in ecosystems. Ceramics are mostly produced using natural materials that contain a high content of clay minerals; hence ceramic wastes can theoretically be used as adsorbents. According to the China Building Ceramics and Sanitary Association, China's ceramic production totaled 10.146 billion m^2 in 2018, and an increasing amount of ceramic wastes are being discharged with the rapid development of the ceramic industry, which causes adverse environmental impacts [32,33]. To realize the recycling of ceramic wastes, it is necessary to explore innovative ways of reusing ceramic wastes. It has been reported that ceramic wastes can be used to treat wastewater [34], but investigations on the adsorption of $\text{NO}_3\text{-N}$ by ceramic wastes are rarely reported.

The present research was performed to prepare a Si–Al porous clay mineral material W (PCMW) as a raw material for ceramics from two kinds of natural clay minerals. The adsorption of $\text{NO}_3\text{-N}$ as a model pollutant in groundwater onto PCMW waste was then evaluated. The structure of PCMW was characterized by scanning electron microscopy (SEM), X-ray fluorescence (XRF), powder X-ray diffraction (XRD), $\text{pH}_{(\text{zpc})}$, Fourier transform infrared spectroscopy (FTIR), and zeta potential analyses. The effects of some basic parameters, such as the contact time, pH, initial concentrations of $\text{NO}_3\text{-N}$, PCMW dosage, the particle size of PCMW, and temperature, on the loading of $\text{NO}_3\text{-N}$ onto PCMW were investigated. In addition, the equilibrium adsorption data were fitted to isotherm models and kinetic models for the determination of constants related to the adsorption phenomena. Thermodynamic studies and ion exchange experiments were also conducted to determine the type of adsorption process. The regeneration and reusability of the adsorbent were also evaluated.

2. Materials and methods

2.1. Adsorbents preparation

PCMW was synthesized from two natural clays, in which the contents of muscovite were 28.1 and 16.9 wt.%, quartz were 15.4 and 10.4 wt.%, potash feldspar were 1.3 and 0.6 wt.%, kaolinite were 55.2 and 72.1 wt.%, respectively. The two natural clays were uniformly mixed in a mixing machine at a mass ratio of 2:7; then, water was added to obtain a uniform mixture. The mixture was aged at room temperature. After drying, the mixture was placed in an electric furnace for firing, the firing temperature of which was 800°C with a heating ramp rate of 40°C/s ; the firing atmosphere was an oxidizing environment, and the firing time was 8 h. Finally, the mixture was naturally cooled to room temperature to obtain a Si–Al porous clay mineral material.

2.2. Characterization methods

Several techniques were employed for the characterization of PCMW. The basic parameters of porous structure include surface area, pore diameter, pore capacity, and pore distribution were characterized by N_2 adsorption–desorption isotherms at 77.35 K using MicroActive for ASAP 2460 (Micromeritics, USA). The specific surface area and pore volume were determined by the Brunauer–Emmett–Teller method. Micropore surface area and limiting micropore volume were the Dubinin–Astakhov methods. The surface morphologies of PCMW were investigated using SEM, operating at an accelerating voltage of 30 kV for photomicrographs (SU8020, HITACHI, Japan), and the samples were initially placed in a vacuum chamber for coating with a thin layer (few nanometers) of gold (Au). The chemical compositions of PCMW were tested by means of XRF by SEA1000S/A (NSK LTD, Japan). XRD experiments were performed with Cu-K α radiation operating at 40 mA and 40 kV between 10° and 90° (2θ) with a step size of 0.02° using ZSXPrimus II (Rigaku Corporation, Japan) and identified using JCPDS files. The contents of PCMW were determined by using the relative intensity ratio (RIR) method. FTIR characterizations were carried out between 400 and $4,000\text{ cm}^{-1}$ by Nicolet FTIR-iS10 (Thermo Fisher Scientific, USA) using KBr pellet technique. The pH at which the surface charge is zero, known as the zero point charge $\text{pH}_{(\text{zpc})}$ is determined using the batch equilibration technique that described in other research [35]. Forty milliliters of KNO_3 solutions (0.01 mol/L) were placed in closed Erlenmeyer flasks; the initial pH (pH_i) of each solution was adjusted in the range from 2 to 14 by adding HCl or NaOH solution (concentration 0.1 mol/L). Then, 0.2 g of PCMW was added and the final pH (pH_f) was measured after 96 h at room temperature in a shaking table. The $\text{pH}_{(\text{zpc})}$ was pH_f vs. pH_i crosses the line at $\text{pH}_f = \text{pH}_i$. Zeta potential was conducted by Zetasizer Nano ZS 90 (Malvern Instruments, UK). Ten milligrams PCMW which was ground to $5\text{ }\mu\text{m}$ was added into 10 mL deionized water and stirred it on a magnetic mixer for 30 min at room temperature. The zeta potential was tested in a range of 2–12 pH. Quality control of all techniques were performed by repeating the detection/experiments three times and average data was used.

2.3. Batch adsorption experiments

Batch experiments consisted of the respective effect of contact time, pH, initial concentrations of $\text{NO}_3\text{-N}$, PCMW dosage, the particle size of PCMW, and temperature on $\text{NO}_3\text{-N}$ from groundwater by PCMW. All batch adsorption experiments were performed in 250 mL Erlenmeyer flask containing 200 mL $\text{NO}_3\text{-N}$ with PCMW specific dosage and shanking at 150 rpm using a shaking table. For the effect of the initial aqueous pH solution varied between 4 and 10, the initial concentration of $\text{NO}_3\text{-N}$ and PCMW dosage were respectively fixed to 20 mg/L and 1 g with the particle size of 1–2 mm. The pH adjustment was done by using 0.1 M HCl and NaOH solutions and the added volume for pH adjustment did not exceed 1% of the solution volume. Seven initial concentrations of $\text{NO}_3\text{-N}$ were chosen, 5, 10, 15, 20, 25, 30, and 40 mg/L, respectively, and each flask was

kept in 1 g of PCMW, the particle size of 1–2 mm and pH of 6.0. The impacts of the dosage of PCMW and particle size of PCMW were determined for a 20 mg/L initial concentration of $\text{NO}_3\text{-N}$ at pH 6.0 while the tested PCMW dosage varied from 0.2 to 4 g and the particle size of PCMW was 2–3, 1–2, 0.5–1, or 0–0.5 mm. Finally, to investigate the thermodynamics of adsorption, experiments were carried out at 15°C, 20°C, 25°C, and 30°C with a 20 mg/L initial concentration of $\text{NO}_3\text{-N}$, pH 6.0 and 1 g of PCMW with a 1–2 mm particle size. The contact time was checked at 4, 8, 24, 48, 72, 96, and 120 h. The $\text{NO}_3\text{-N}$ concentration in groundwater was determined by the spectrophotometric method carried out with a UV-vis spectrophotometer at 420 nm (photoLab 7600, WTW, Germany). Quality control testing included experiments with blanks and duplicates. Each experiment was made at least in triplicate.

At a giving time (t), the amount of adsorbed $\text{NO}_3\text{-N}$ onto PCMW, Q_t (mg/g), was calculated through the following equation:

$$Q_e = \frac{(C_0 - C_e)V}{M} \quad (1)$$

where C_0 (mg/L) and C_e (mg/L) are respectively the initial and equilibrium concentration at time t the concentration of $\text{NO}_3\text{-N}$ in groundwater, V (L) is the volume of the groundwater, and M (g) is the mass of PCMW.

2.4. Co-existing ions experiment

Based on the class V requirement of quality standard for groundwater (GB/T 14848-93), NO_2^- (0.1 mg/L), Cl^- (350 mg/L), F^- (2 mg/L), HCO_3^- (200 mg/L), CO_3^{2-} (200 mg/L), SO_4^{2-} (350 mg/L), NH_4^+ (0.5 mg/L), Fe^{2+} (1.50 mg/L), Mn^{2+} (1 mg/L) was added to 200 mL deionized water with 30 mg/L $\text{NO}_3\text{-N}$, respectively. The contents of $\text{NO}_3\text{-N}$ were measured after 72 h under the conditions pH 6.0, 2 g PCMW with 1–2 mm particle size, room temperature, 150 rpm.

2.5. Leaching and regeneration experiment

The adsorbed PCMW was added to 200 mL deionized water for 150 rpm, 25°C, and 24 h, then PCMW was moved to 20 mg/L $\text{NO}_3\text{-N}$, $\text{NO}_3\text{-N}$ content in groundwater was measured after shaking at 150 rpm, pH 6.0, 25°C for 120 h. The stability of PCMW was evaluated in several consecutive experiments by repeating adsorption and leaching experiments. The removal rates after each adsorption experiment were measured. At a giving number of times (n), the removal rate (%) of $\text{NO}_3\text{-N}$ was calculated through the following equation:

$$\text{Removal rate (\%)} = \frac{(C_0 - C_n)}{C_0} \times 100 \quad (2)$$

where C_0 (mg/L) and C_n (mg/L) are, respectively, the initial and at a giving number of times the concentrations of $\text{NO}_3\text{-N}$ in groundwater.

2.6. Adsorption kinetics and isotherm models

As shown in Table 1, the five adsorption kinetic models (pseudo-first-order, pseudo-second-order, Elovich, intra-particle diffusion, and liquid film diffusion models) and five isothermal models (Langmuir, Freundlich, Dubinin–Radushkevich, Temkin, and Toth models) were used to evaluate the kinetic and isotherm models for adsorption of $\text{NO}_3\text{-N}$ onto PCMW.

3. Results and discussion

3.1. Factors affecting the adsorption of $\text{NO}_3\text{-N}$ onto PCMW

3.1.1. Effects of pH and zeta potentials

The pH of groundwater is an important parameter in the adsorption process due to its effects on the ion concentration on the surface, solubility of the solute, degree of ionization, and functional groups of the adsorbent [36,37]. It is observed that the adsorption capacity of PCMW decreased with increasing pH, which may be explained based on $\text{pH}_{(\text{zpc})} = 6.27$ and $\text{pH}_{(\text{ipc})} = 6.41$ (Fig. 1). $\text{pH}_{(\text{zpc})}$ is an important parameter for explaining the attraction of ions on the adsorbent surface during the adsorption process. The surface charge of PCMW was positive below $\text{pH}_{(\text{zpc})}$, thereby attracting $\text{NO}_3\text{-N}$. The zeta potential of PCMW changed from positive to negative at the isoelectric point, where the zeta potential of the surface of PCMW is zero. The zeta potential of PCMW decreased with increasing pH, and the adsorption capacity decreased from 4.64 mg/g at pH 4 to 2.25 mg/g at pH 10. The zeta potentials were positive less than $\text{pH}_{(\text{ipc})} = 6.41$ (pH at the isoelectric point charge), and the positively charged surface could provide the driving force for the electrostatic interaction with $\text{NO}_3\text{-N}$. Therefore, as the pH of the aqueous solution increased, the competition for adsorption/exchange sites on the surface intensified and was not conducive to adsorption/electrostatic attraction [38]. Increasing pH decreased the adsorption capacity, which was caused by an increase of the electrostatic repulsion between the surface charges of PCMW and $\text{NO}_3\text{-N}$ in groundwater.

3.1.2. Effects of the initial concentration of $\text{NO}_3\text{-N}$ and contact time

The effect of the initial $\text{NO}_3\text{-N}$ concentration is shown in Fig. 2, the trends for each initial concentration were similar. The adsorption capacity of PCMW increased over time, reaching a maximum after 120 h of contact time and then tending toward a constant value. The adsorption capacity of PCMW (1.70–3.89–4.49 mg/g) increased with the increasing initial $\text{NO}_3\text{-N}$ concentration (5–20–40 mg/L), and the increase of the adsorption capacity slowed with the increasing initial $\text{NO}_3\text{-N}$ concentration, which indicated the gradual steps to the saturation of the adsorbent with $\text{NO}_3\text{-N}$ molecules. As the driving force increased with the initial $\text{NO}_3\text{-N}$ concentration, adsorption needed to overcome more mass transfer resistance between the solute phase and adsorbent phase [39]. The adsorption was easy and fast in the initial stage, in which $\text{NO}_3\text{-N}$ was adsorbed on the external surface area of PCMW. Then the external surface was saturated, blocking the adsorptive sites; $\text{NO}_3\text{-N}$

Table 1
Adsorption isotherm and kinetic models used in this study

	Models name	Equations
Kinetic models	Pseudo-first-order	$Q_t = Q_e (1 - \exp(-K_1 t))$
	Pseudo-second-order	$Q_t = \frac{K_2 Q_e^2 t}{1 + K_2 Q_e t}$
	Elovich	$Q_t = \left(\frac{1}{b}\right) \ln ab + \left(\frac{1}{b}\right) \ln t$
	Intra-particle diffusion	$Q_t = K_i \sqrt{t} + C_i$
	Liquid film diffusion	$\ln(1 - F) = -K_{fd} t, F = \frac{Q_t}{Q_e}$
	Langmuir	$Q_e = \frac{Q_m K_L C_e}{1 + K_L C_e}, R_L = \frac{1}{1 + K_L C_0}$
Isotherm models	Freundlich	$Q_e = K_F C_e^{\frac{1}{n}}$
	Dubinin–Radushkevich	$Q_e = Q_s \exp \left[\frac{\left(RT \ln \left(1 + \frac{1}{C_e} \right) \right)^2}{-2E^2} \right]$
	Temkin	$Q_e = \frac{RT}{b_T} \ln(K_{Te} C_e)$
	Toth	$Q_e = \frac{Q_m K_{To} C_0}{\left(1 + (K_{To} C_0)^t \right)^{\frac{1}{t}}}$

where Q_t (mg/g) is the adsorption capacity at time t , Q_e (mg/g) is the adsorption capacity at equilibrium time, K_1 (1/h) is the rate constant of pseudo-first-order, t (min) is the time; K_2 (1/h) is the rate constant of pseudo-second-order; a is the rate constant of chemisorption, b is the constant of the surface coverage related to the activation energy for chemisorption; K_i (mg min^{0.5}/g) is the intra-particle diffusion rate constant, C_i (mg/g) is a constant; K_{fd} is the adsorption rate constant.

Where Q_e (mg/g) is the adsorption capacity at equilibrium time; Q_m (mg/g) is the maximum adsorption capacity, K_L (L/mg) is the Langmuir constant, C_e (mg/L) is the equilibrium concentration, R_L is the separation constant, C_0 (mg/L) is the initial concentration; K_F ((mg/g)/(mg/dm³)^{1/n}) and n are the Freundlich constants; Q_s (mg/g) is the maximum adsorption capacity, R (8.314 J/mol K) is the gas constant, T (K) is the absolute temperature, E (kJ/mol) is energy of adsorption; b_T is the Temkin constant, K_{Te} (L/mg) is the equilibrium bond constant related to the maximum energy of bond; K_{To} is the Toth constant.

entered the pores and adsorbed on the internal surface of PCMW, which took a long time.

3.1.3. Effect of the PCMW dosage

The adsorption capacity of PCMW and the removal rate of NO₃-N increased with the increase of the PCMW dosage from 0.5 to 1.5 g. The removal rate of NO₃-N no longer increased and the adsorption capacity of PCMW decreased significantly when the PCMW dosage increased from 1.5 to 4.0 g (Fig. 3). These results indicate that the best PCMW dosage for adsorption was 1.5 g, preventing the use of excess adsorbent. These phenomena could be attributed to an

increased number of active surface sites for NO₃-N adsorption. When the PCMW dosage was greater than 2.0 g, the increase of the PCMW dosage at a constant concentration of NO₃-N reduced the complete surface area of PCMW and caused the accumulation of active sites of PCMW, which limited the accessibility of other NO₃-N adsorbed to the surface [40,41]. Therefore, the removal rate of NO₃-N remained unchanged after a significant enhancement.

3.1.4. Effect of particle size of PCMW

Fig. 4 shows the effect of the particle size of PCMW on NO₃-N adsorption. The adsorption capacity of PCMW

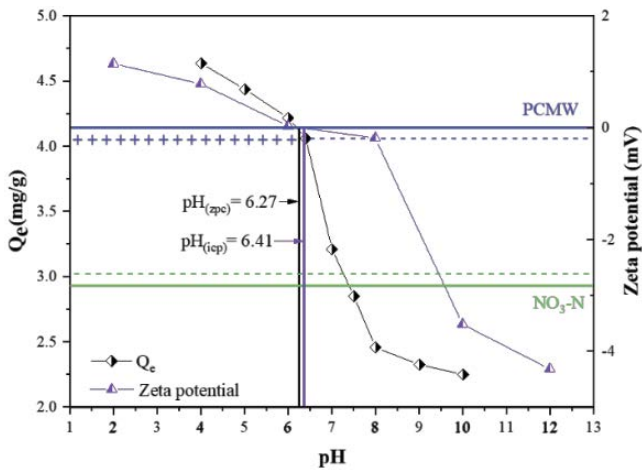


Fig. 1. Effect of pH on adsorption and zeta potential of PCMW as a function of pH.

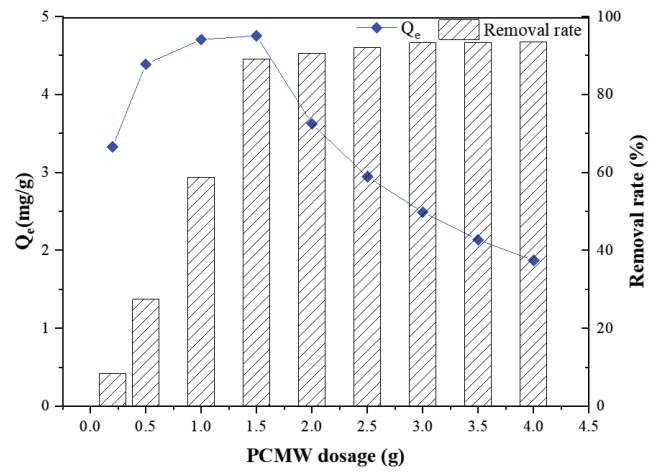


Fig. 3. Effect of PCMW dosage and PCMW particle size on adsorption.

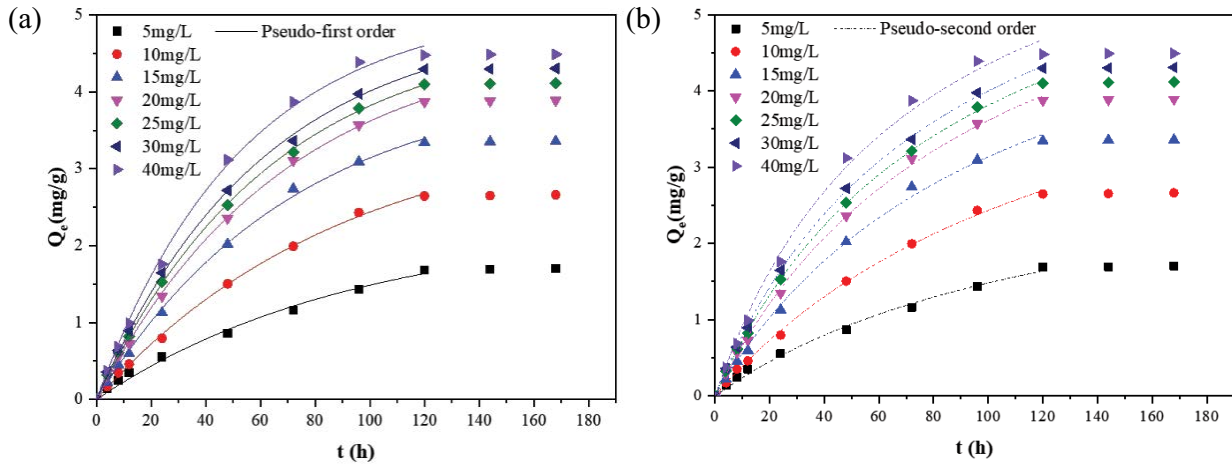


Fig. 2. Effect of initial concentrations and contact time on adsorption; pseudo-first-order and pseudo-second-order for adsorption, pseudo-first-order (a) and pseudo-second-order (b).

Table 2
Adsorption parameters of the kinetic models

Experiment	C_0 (mg/L)	5	10	15	20	15	30	40
	$Q_e(\text{exp})$ (mg/g)	1.71	2.67	3.36	3.89	4.12	4.31	4.49
	$K_1 \times 10^3$ (1/h)	10.61	11.02	13.85	14.51	15.54	16.46	18.82
Pseudo-first-order	$Q_e(\text{cal})$ (mg/g)	2.27	3.65	4.19	4.72	4.85	4.97	5.14
	R^2	0.992	0.999	0.999	0.999	0.999	0.999	0.998
	$K_2 \times 10^3$ (1/h)	1.12	1.25	1.43	1.48	1.57	1.67	1.90
Pseudo-second-order	$Q_e(\text{cal})$ (mg/g)	3.49	5.80	6.43	7.15	7.18	7.28	7.44
	R^2	0.993	0.999	0.997	0.996	0.999	0.999	0.995
	a	0.10	0.15	0.20	0.24	0.26	0.27	0.30
Elovich	b	2.25	1.32	1.02	0.90	0.86	0.82	0.75
	R^2	0.931	0.968	0.952	0.954	0.961	0.964	0.967
Intra-particle diffusion	K_i (mg min ^{0.5} /g)	0.17	0.29	0.37	0.42	0.44	0.46	0.50
	R^2	0.993	0.994	0.992	0.994	0.996	0.96	0.981
Liquid film diffusion	$K_{fd} \times 10^3$	17.91	19.41	21.12	21.23	21.54	21.97	24.88
	R^2	0.980	0.981	0.985	0.988	0.991	0.992	0.989

increased with increasing particle size but hardly changed after the particle size was 1–2 mm. The total surface area of PCMW was composed of the internal and external surface areas covering the pores and channels of the materials, while the external surface area only represented a small part of the total surface area. The external surface area exposed to $\text{NO}_3\text{-N}$ increased as the particle size decreased; thus, the initial adsorption rate increased. However, with the saturation of the adsorption sites, the internal part became more effective for adsorption. However, the surface area only slightly increased when the particle size decreased, while the internal surface area did not have much influence. The number of adsorption sites remained almost unchanged as the particle size increased from 1 to 2 mm; therefore, the equilibrium adsorption capacity did not change with the increase in particle size.

3.1.5. Effect of co-existing ions on adsorption

Other ions, such as NO_2^- , Cl^- , F^- , HCO_3^- , CO_3^{2-} , SO_4^{2-} , NH_4^+ , Fe^{2+} , and Mn^{2+} , coexist with $\text{NO}_3\text{-N}$ in groundwater and have a destructive influence on the $\text{NO}_3\text{-N}$ adsorption process. All of these ions had a negative impact on $\text{NO}_3\text{-N}$ removal, the most adverse of all the coexisting ions was SO_4^{2-} , followed by CO_3^{2-} , and HCO_3^- (Fig. 5). The other negative ions and the positive ions had slightly negative effects on $\text{NO}_3\text{-N}$ removal. The equivalences of the divalent anions SO_4^{2-} and CO_3^{2-} were higher than that of the monovalent anion $\text{NO}_3\text{-N}$ because the greater charge the anions carried in the electrostatic interaction, the stronger the adsorption at the opposite charge point on the surface of the adsorbent [42]. Therefore, PCMW had a greater tendency to adsorb the divalent anions than $\text{NO}_3\text{-N}$. In addition, HCO_3^- competed with $\text{NO}_3\text{-N}$ to be trapped by PCMW and subsequently reduced the $\text{NO}_3\text{-N}$ removal rate.

3.2. Adsorption characteristics of $\text{NO}_3\text{-N}$ onto PCMW

3.2.1. Adsorption kinetics

To further investigate the adsorption behavior, the adsorption kinetics were studied because they not only described the adsorption rate but also indicated the mechanism of the adsorption process. The pseudo-first-order model was mostly adapted for the weakest concentrations of the aqueous solution. The pseudo-second-order model assumes that chemisorption is dominant and controls the adsorption as a rate-limiting step, and the intraparticle diffusion model was used to identify the diffusion mechanism. The equilibrium adsorption capacities of PCMW, as functions of the different initial $\text{NO}_3\text{-N}$ concentrations, are presented in Fig. 2. Since adsorption did not continue after 120 h, the pseudo-first and pseudo-second-order models were fitted within 0 to 120 h. Fig. 6 shows the Elovich, liquid film diffusion, and intraparticle diffusion models, and the results of all the kinetic models are shown in Table 2.

The correlation coefficient (R^2) and comparison of the difference between the equilibrium adsorption capacity of the test value $Q_e(\text{exp})$ and the calculated value $Q_e(\text{cal})$ in the fitting results show that the pseudo-first-order model was the best-fit model for $\text{NO}_3\text{-N}$ adsorption onto PCMW

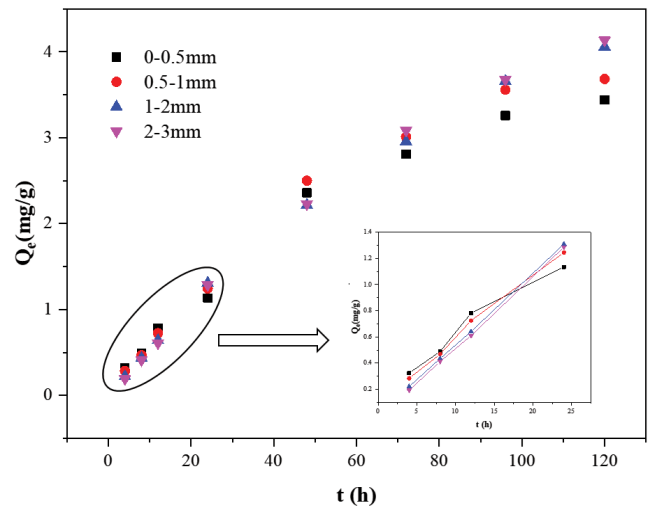


Fig. 4. Effect of PCMW particle size on adsorption.

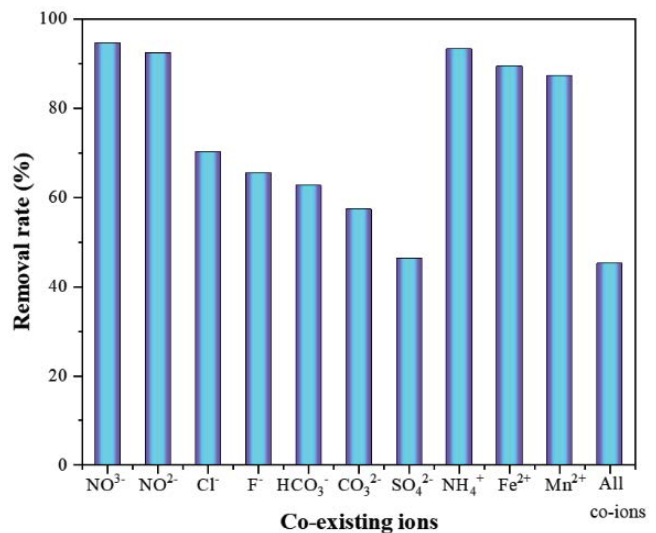


Fig. 5. Effects of different co-existing ions on adsorption.

($R^2 > 0.99$; the difference between $Q_e(\text{exp})$ and $Q_e(\text{cal})$:14.48 is -43.36%). The R^2 values of the Elovich model were 0.93–0.99; the applicability of this model also suggests that the adsorption process was based on the physical characteristics of the adsorbent system. Combining with the results presented above, the adsorption process involved electrons exchanged between the adsorbent and the adsorbate, and $\text{NO}_3\text{-N}$ was attached to surface of PCMW via physical bonds, such as van der Waals forces and electrostatic interactions [43,44]. All the adsorption rate constants, K_1 , K_2 , K_p and K_{id} , increased with the increasing initial concentration, whereas the degree of the rate constants first increased and then decreased with the initial concentration. At the early stage of adsorption, the curves for the intraparticle diffusion model did not pass through the origin, while the liquid film diffusion models were well fitted to the experimental data ($R^2 > 0.98$). Therefore, both intraparticle diffusion and liquid film diffusion were the rate-controlling steps; both were the

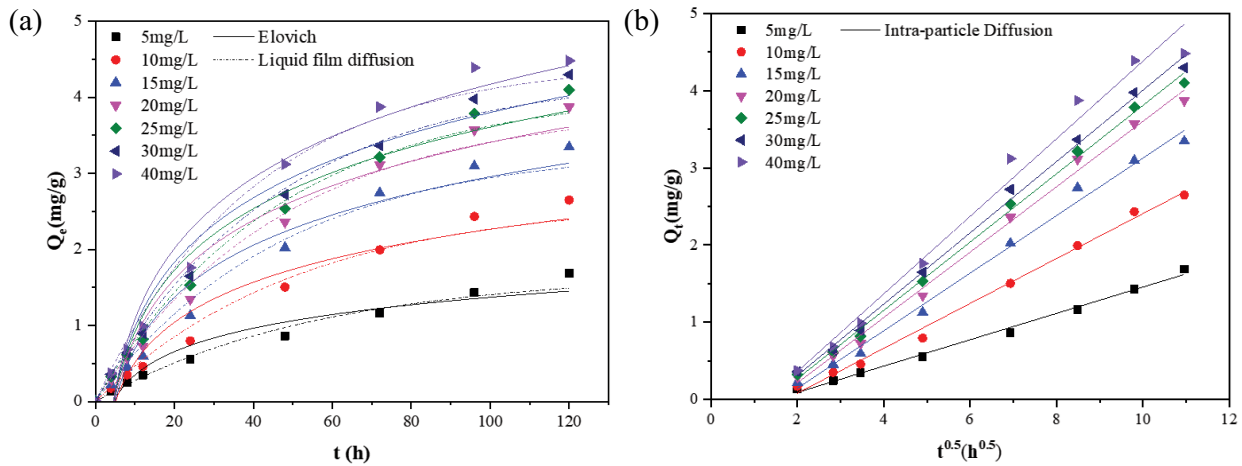


Fig. 6. Adsorption kinetics of $\text{NO}_3\text{-N}$ onto PCMW, Elovich, and liquid film diffusion (a) and intra-particle diffusion (b).

major limitations for the adsorption of $\text{NO}_3\text{-N}$ onto PCMW [45,46]. It can be speculated that four steps are involved in the adsorption process: step 1, $\text{NO}_3\text{-N}$ was transported from the aqueous solution to the external layer of PCMW, which was a nonlimiting step; step 2, $\text{NO}_3\text{-N}$ diffused across the external film surrounding PCMW; step 3, $\text{NO}_3\text{-N}$ diffused into the pores of PCMW; and step 4, $\text{NO}_3\text{-N}$ adsorbed onto the external and internal surface of PCMW due to physical interactions.

3.2.2. Adsorption isotherms

The adsorption isotherm related to the adsorption of molecules on a solid surface to its concentration above the solid surface at a constant temperature and also indicated the efficiency of the adsorbent in the adsorption process. The equilibrium adsorption capacities as functions

of the different temperatures are presented in Fig. 7. This figure shows five fitting curves for the isotherm models, and the parameters of the models are shown in Table 3. The R^2 values of the five isotherms were ranked as follows: Langmuir (0.995–0.999) > Dubinin–Radushkevich (0.990–0.998) > Temkin (0.973–0.995) > Freundlich (0.909–0.944) > Toth (0.887–0.920). The Dubinin–Radushkevich isotherm typically describes an adsorption mechanism with a Gaussian energy distribution onto a heterogeneous surface, which is used as a criterion to distinguish between physisorption ($E < 8$ kJ/mol) and chemisorption ($E > 8$ kJ/mol) [47]. $E = 3.92\text{--}5.30$, which indicated that the adsorption of $\text{NO}_3\text{-N}$ onto PCMW was via physisorption, consistent with the results of the adsorption kinetics. The Toth and Temkin isotherms were suitable to characterize the multilayer adsorption; thus, the adsorption of $\text{NO}_3\text{-N}$ onto PCMW was monolayer adsorption, and there was a

Table 3
Adsorption parameters of the isotherms models

Experiment	T (K)	283	288	298	303
	$Q_e(\text{exp})$ (mg/g)	1.47	2.89	3.90	4.48
	$K_L \times 10^3$ (L/mg)	35.69	46.62	51.56	60.43
Langmuir	$Q_e(\text{cal})$ (mg/g)	1.76	3.16	4.54	5.30
	R^2	0.999	0.995	0.997	0.995
	$K_F ((\text{mg/g})/(\text{mg}/\text{dm}^3)^{1/n})$	0.24	0.69	0.86	1.03
Freundlich	N	1.99	2.45	2.33	2.40
	R^2	0.944	0.909	0.929	0.933
	$Q_e(\text{cal})$ (mg/g)	1.80	3.40	4.66	5.30
Dubinin–Radushkevich	E (kJ/mol)	3.92	5.15	5.02	5.30
	R^2	0.996	0.998	0.995	0.990
	$b_T \times 10^{-3}$	4.524	2.640	1.956	1.782
Temkin	$K_{Te} \times 10^3$ (L/mg)	459.08	699.63	633.9	685.2
	R^2	0.995	0.973	0.984	0.983
	$Q_e(\text{cal})$ (mg/g)	1.35	2.66	3.64	4.18
Toth	$K_{To} \times 10^3$	51.49	63.33	58.53	58.76
	R^2	0.920	0.887	0.896	0.894

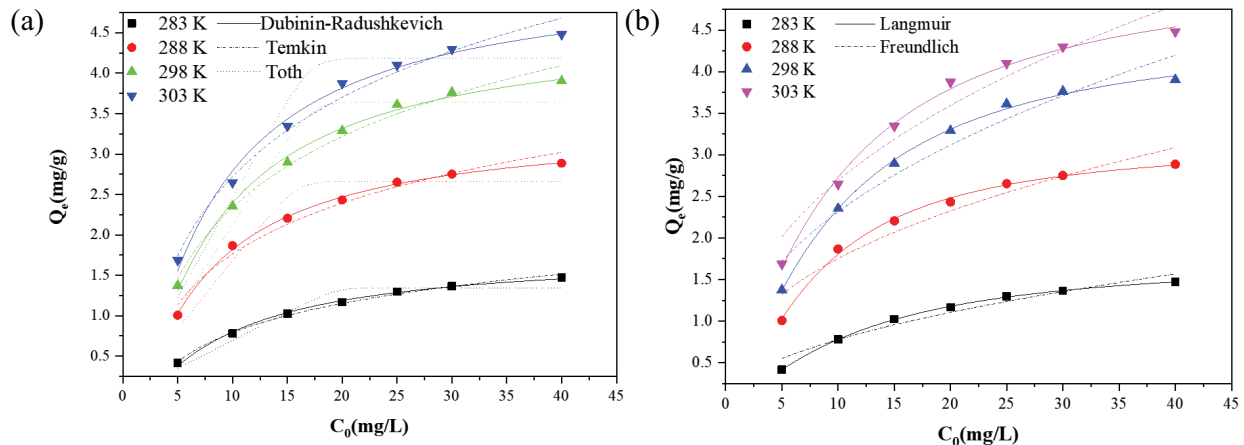


Fig. 7. Adsorption isotherms of $\text{NO}_3\text{-N}$ onto PCMW at different temperatures, Langmuir, and Freundlich (a) and Dubinin–Radushkevich, Temkin, and Toth (b).

uniform distribution of $\text{NO}_3\text{-N}$ on the surface of PCMW [49]. The adsorption isotherm of the adsorption of $\text{NO}_3\text{-N}$ onto PCMW was the *L*-type isotherm, and the slope did not increase with the increase of the initial $\text{NO}_3\text{-N}$ concentration, indicating a high relative affinity of PCMW to $\text{NO}_3\text{-N}$ at a low $\text{NO}_3\text{-N}$ concentration. The values of n from the Freundlich isotherm were from 1.99 to 2.40, which were >1 , indicating that the adsorption of $\text{NO}_3\text{-N}$ onto PCMW was favorable [50]. According to the Langmuir and Dubinin–Radushkevich isotherms, the maximum adsorption capacity for both was 5.30 mg/g at 303 K.

3.2.3. Effect of temperature and the thermodynamic study

The adsorption capacity of PCMW increased with the increasing initial concentrations, and the increasing temperatures showed the endothermic feature of $\text{NO}_3\text{-N}$ adsorption onto PCMW (Fig. 8). The enhancement of $\text{NO}_3\text{-N}$ adsorption with increasing temperature was essentially caused by the increase of surface activity [51]. At low temperatures, increasing the temperature accelerated the adsorption rate and increased the adsorption capacity. The adsorption of $\text{NO}_3\text{-N}$ onto PCMW was endothermic according to $\Delta H^\circ > 0$ (Table 4), so the increasing temperature accelerated the increasing rate of adsorption capacity when the adsorption equilibrium was about to be reached.

Insights regarding the adsorption mechanism can be interpreted from the thermodynamic parameters namely Gibbs free energy ΔG° (kJ/mol), enthalpy ΔH° (kJ/mol), and

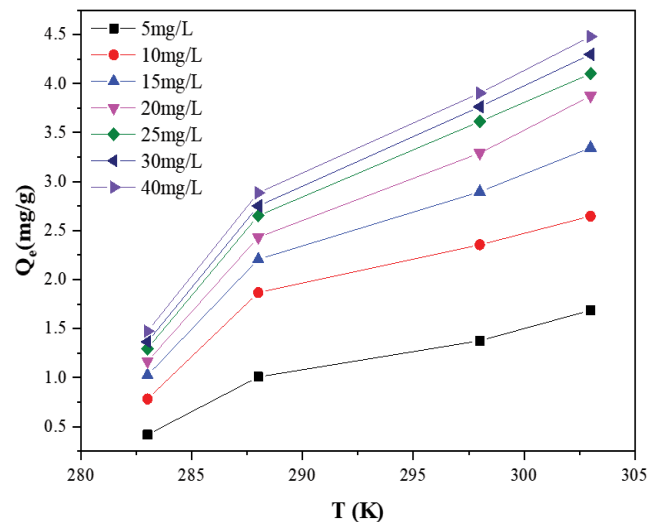


Fig. 8. Effect of temperatures on adsorption.

entropy ΔS° (kJ/mol K). The thermodynamic equilibrium constant K and other thermodynamic parameters were determined from the following equations:

$$\Delta G^\circ = -RT \ln K_c \quad (3)$$

$$\Delta G^\circ = \Delta H^\circ - T\Delta S^\circ \quad (4)$$

Table 4
Thermodynamic parameters for the (IC) adsorption onto AC

C_0 (mg/L)	ΔG° (kJ/mol)				ΔH° (kJ/mol)	ΔS° (kJ/mol·K)	E_a (kJ/mol)
	283 K	288 K	298 K	303 K			
5	-7.33	-7.94	-9.25	-9.89	28.89	0.128	20.40
20	-7.79	-8.35	-9.46	-10.01	23.62	0.111	25.54
40	-8.38	-8.84	-9.75	-10.20	17.37	0.091	34.37

$$\ln K_c = \frac{\Delta S^\circ}{R} - \frac{\Delta H^\circ}{R} \frac{1}{T} \quad (5)$$

$$\ln K = \ln A - \frac{E_a}{RT} \quad (6)$$

where R (8.314 J/mol K) is the universal gas constant, K_c is the equilibrium constant which was from Langmuir, K is the rate constant which was from pseudo-first-order models, A is the Arrhenius constant, E_a (kJ/mol) is the activation energy. Three concentrations of 5, 20, and 40 mg/L were selected to fit in the range of 283–303 K, the values of ΔG° , ΔH° , ΔS° , and E_a could be determined by plotting $\ln K_c$ and $\ln K$ vs. $1/T$ which were linear (Fig. 9), and the results were given in Table 4.

A negative ΔG° indicates a spontaneous and feasible process in nature, and the values of ΔG° decreased with increasing temperature and initial concentrations of $\text{NO}_3\text{-N}$, pinpointing a favorable adsorption process at a higher temperature. In particular, ΔH° was less than 40 kJ/mol since the forces involved in the physical adsorption were weak. The forces involved in the chemical adsorption were stronger than those involved in the physical adsorption, so the ΔH° of chemical adsorption was 40–100 kJ/mol [52]. The ΔH° values were 17.37–28.89 kJ/mol, indicating that the adsorption of $\text{NO}_3\text{-N}$ onto PCMW was physical adsorption. The positive value of ΔS° showed the increased randomness at the solid–liquid interface during the adsorption process. The magnitude of E_a also gave an indication of whether the type of adsorption was a physical or chemical process. E_a of physical adsorption is 5–40 kJ/mol, whereas 40–800 kJ/mol is characteristic of chemical adsorption [53]. The values of E_a were found to be 20.40–34.37 kJ/mol, implying physical adsorption as well.

3.3. Characterization of PCMW and removal mechanism

3.3.1. XRF analysis and basic parameters of PCMW

The chemical components of PCMW by XRF analysis were: 54.10 wt.% SiO_2 , 32.14 wt.% Al_2O_3 , 7.74 wt.% Fe_2O_3 ,

3.13 wt.% K_2O , 1.41 wt.% Ti_2O_3 , 0.41 wt.% CaO , 0.37 wt.% MgO , 0.15 wt.% Na_2O , and 0.55 wt.% impurities. The adsorption/desorption isotherms recorded on PCMW adsorption revealed a characteristic tight hysteresis loop at high relative pressures (Fig. 10), $p/p_0 = 0.94$, which pointed to the presence of mesopores [37]. The specific surface area (S_{BET}) of PCMW was 63.52 m^2/g , the total pore volume was 0.25 cm^3/g and the average pore size was 4.06 nm. PCMW had a good affinity for $\text{NO}_3\text{-N}$ as S_{BET} and pore volume were large. Investigation of the pore size distribution using Barrett–Joyner–Halenda (BJH) analysis showed that the pore size distribution was 5.12–6.92 nm, in the mesopore range 5–50 nm. Due to the small $\text{NO}_3\text{-N}$ ionic radius, PCMW were conducive to $\text{NO}_3\text{-N}$ penetration into the internal [38].

3.3.2. SEM analysis

SEM images of PCMW before and after adsorption are shown in Fig. 11. The apparent mesoporous structure of PCMW could be observed on the surface and inside of

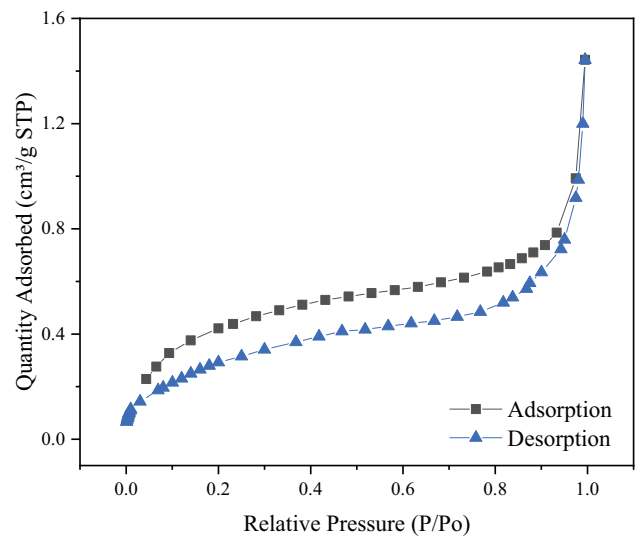


Fig. 10. Nitrogen adsorption–desorption isotherms for PCMW.

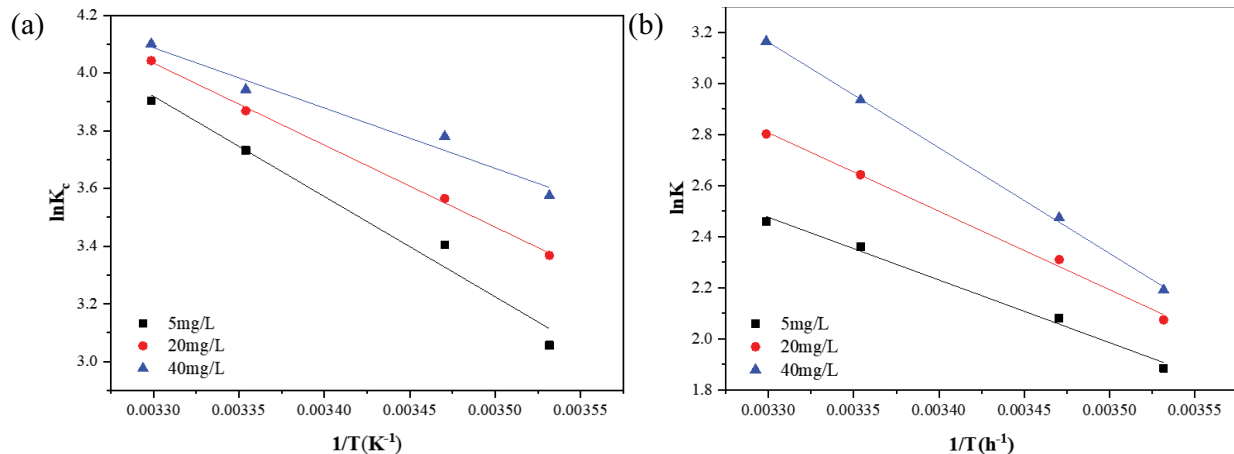


Fig. 9. Thermodynamic curve for adsorption of $\text{NO}_3\text{-N}$ on PCMW, ΔH° and ΔS° (a) and E_a (b).

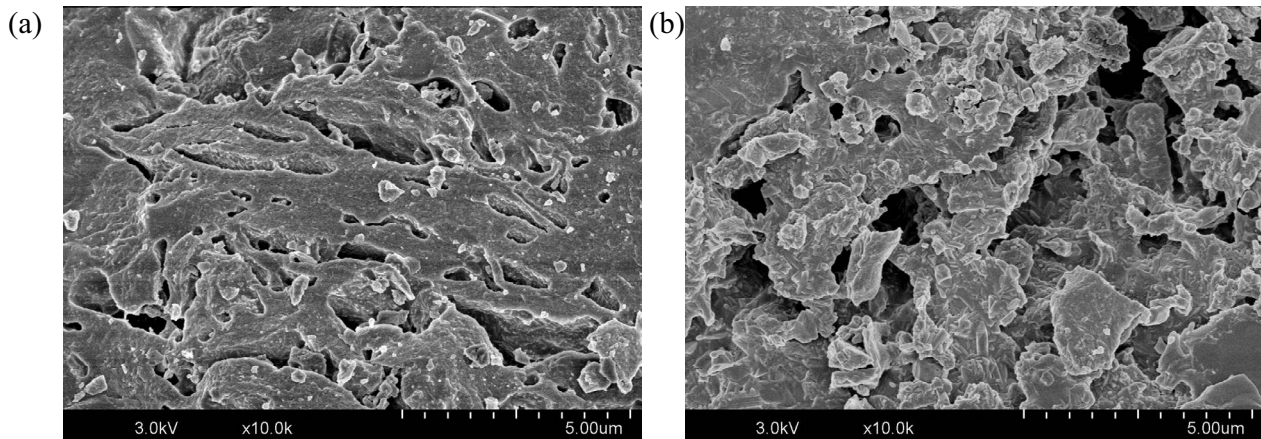


Fig. 11. SEM of PCMW before and after adsorption, before adsorption (a) and after adsorption (b).

PCMW. The mean diameter of the pores was approximately 10 nm, which was highly consistent with the BJH pore size of PCMW. Due to the porous, irregular, and uneven structure of the material, $\text{NO}_3\text{-N}$ could be easily captured by the active sites of PCMW, allowing the adsorption system to reach equilibrium with a relatively large adsorption capacity when aqueous solution diffused into the interior of PCMW. A difference in the surface of PCMW was observed, in which irregular protrusions and a heterogeneous morphology appeared on the solid surface after adsorption, which were attributed to the swelling effects of the clay minerals during the process.

3.3.3. XRD analysis

Fig. 12 shows the XRD profiles of PCMW before and after adsorption. Through XRD measurements and the RIR method, PCMW before adsorption was shown to be composed of quartz (56.3 wt.%), mullite (34.6 wt.%), moganite (5.1 wt.%), sillimanite (2.5 wt.%), and impurities (1.5 wt.%). After adsorption, the main characteristic peak shift was

within 1 Å. Hence, little change of the XRD patterns of PCMW occurred during adsorption.

3.3.4. FTIR analysis

FTIR revealed the type of molecular interactions between $\text{NO}_3\text{-N}$ and PCMW. This study was also conducted to evaluate the roles of the functional groups on the surface of PCMW in the adsorption process. FTIR spectra of PCMW before and after the adsorption are presented in Fig. 13. The bands at 2,369.74 and 2,368.26 cm^{-1} were due to the stretching vibration of Si–H, and the bands in the 1,089.15 cm^{-1} region correspond to the stretching vibration of Si–O. The appearance of a strong bending vibrational band (after adsorption) at 1,384.22 cm^{-1} was ascribed to the stretching vibration of the N–O bond, which represented the occurrence of $\text{NO}_3\text{-N}$ adsorption on PCMW [38]. The adsorption band for -NH_2 at 896.29 shifted to 896.78 cm^{-1} after adsorption and its intensity decreased [54], which indicated that $\text{NO}_3\text{-N}$ interacted with amine groups through electrostatic interactions during the adsorption

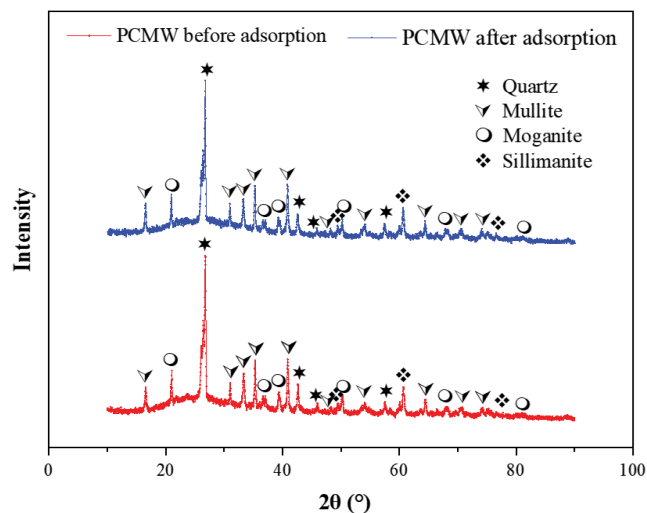


Fig. 12. XRD patterns of PCMW before and after adsorption.

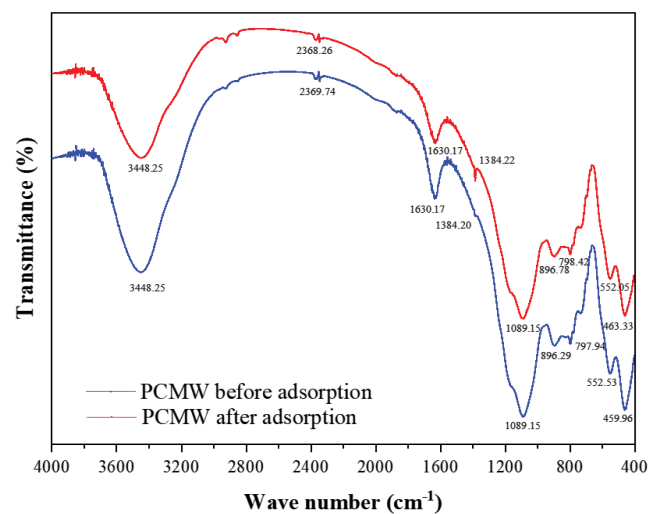


Fig. 13. FTIR spectra of PCMW before and after adsorption.

process (Eq. 7). Additionally, the adsorption bands for the bending vibrations of Al–OH–Mg at 797.94 shifted to 798.42 cm^{-1} [53], the stretching vibration of Fe–O at 552.53 shifted to 552.05 cm^{-1} [36], and the stretching vibration and bending vibration of Si–O–Al at 459.96 shifted to 463.33 cm^{-1} [37,55], which indicated that $\text{NO}_3\text{-N}$ adsorbed onto PCMW via electrostatic interactions. Meanwhile, the bands at 3,448.25 cm^{-1} were due to stretching of O–H, while the 1,630.17 cm^{-1} was due to the bending of O–H, which might be caused by the water molecules coordinated to PCMW, causing the overlap of a hydroxyl group from the adsorption of water [56]. The intensity of the stretching of O–H decreased and the intensity of the bending of O–H increased after adsorption, which implied that the surrounding environment of hydroxyl groups and water molecules changed after adsorption and that there was nearly no water in the interlayer space, indicating the inclusion of $\text{NO}_3\text{-N}$ onto PCMW [37]. Hence, it could be concluded that the water adsorption process on PCMW and the electrostatic interactions between $\text{NO}_3\text{-N}$ and O–H could also contribute to the $\text{NO}_3\text{-N}$ adsorption process.



3.4. Regeneration of PCMW

To evaluate the stability and availability of PCMW, it was reused in six consecutive experiments. The values of ΔG° were found to be less than 5 J/mol, which indicated that the adsorbent PCMW was easily regenerated [57]. As Fig. 14 shows, the $\text{NO}_3\text{-N}$ removal rates slightly decreased with the successive cycles. After the second cycle, the removal rate was 89.34%, and the other cycles were similar to that of cycle 3. The results indicated that cyclic use of PCMW is feasible.

3.5. Comparison of PCMW with other adsorbents

The adsorption capacities of various adsorbents toward $\text{NO}_3\text{-N}$ as reported in other studies are presented in Table 5. Comparing the results showed that PCMW was a better adsorbent for $\text{NO}_3\text{-N}$ compared to other adsorbents. Therefore, it could be safely concluded that the PCMW

Table 5

Comparison of adsorption capacity of PCMW to $\text{NO}_3\text{-N}$ with other adsorbents

Adsorbents	Q_{max} (mg/g)	pH	References
Biochars	0.79	<7	[58]
Sediments	1.75	6	[38]
Ion exchange resin	3.17	7	[19]
Sepiolite	3.46	5.6	[59]
Metal impregnated alumina	3.89	7.5	[50]
PCMW	4.49	6	In this study
Corn stalks	13.61	6.8	[60]

has considerable potential for the removal of $\text{NO}_3\text{-N}$ from groundwater.

4. Conclusions

A Si–Al porous clay mineral material W (PCMW) was prepared and characterized as quartz/mullite. PCMW had a high nitrate ($\text{NO}_3\text{-N}$) removal performance as an adsorbent. The adsorption process could be described by the Langmuir isotherm and pseudo-first-order kinetic model, and both intraparticle diffusion and liquid film diffusion could affect the adsorption process. In addition, the Toth and Temkin models indicated a monolayer and uniform distribution of $\text{NO}_3\text{-N}$ on the internal and external surfaces of PCMW. The pseudo-first-order kinetic model, Elovich model, Dubinin–Radushkevich isotherm, ΔH° and E_a from the thermodynamic analysis, zeta potential measurements, and FTIR spectra demonstrated that the adsorption of $\text{NO}_3\text{-N}$ onto PCMW was physical adsorption. The maximum removal rate of $\text{NO}_3\text{-N}$ and maximum adsorption capacity of monolayer adsorption were 96.69% and 4.49 mg/g, respectively. Thermodynamic analysis proved that the adsorption of $\text{NO}_3\text{-N}$ onto PCMW was spontaneous and endothermic. PCMW is composed of natural clay minerals, making it an environmentally benign, useful, recyclable, and economical adsorbent for the efficient adsorption of $\text{NO}_3\text{-N}$ from groundwater.

Acknowledgment

The present work was supported by funds from the Major Science and Technology Program for Water Pollution Control and Treatment (2013ZX07202-010-05).

References

- [1] Z. Yang, J. Chen, H. Li, H. Jin, S. Gao, Z. Ji, Y. Zhu, L. Ran, J. Zhang, Y. Liao, Y. Bai, Sources of nitrate in Xiangshan Bay (China), as identified using nitrogen and oxygen isotopes, *Estuarine Coastal Shelf Sci.*, 207 (2018) 109–118.
- [2] C.W. Drake, C.S. Jones, K.E. Schilling, A.A. Amado, L.J. Weber, Estimating nitrate-nitrogen retention in a large constructed wetland using high-frequency, continuous monitoring and hydrologic modeling, *Ecol. Eng.*, 117 (2018) 69–83.
- [3] T. Darwish, T. Atallah, R. Francis, C. Saab, I. Jomaa, A. Shaaban, H. Sakka, P. Zdruli, Observations on soil and groundwater contamination with nitrate: a case study from Lebanon-East Mediterranean, *Agric. Water Manage.*, 99 (2011) 74–84.

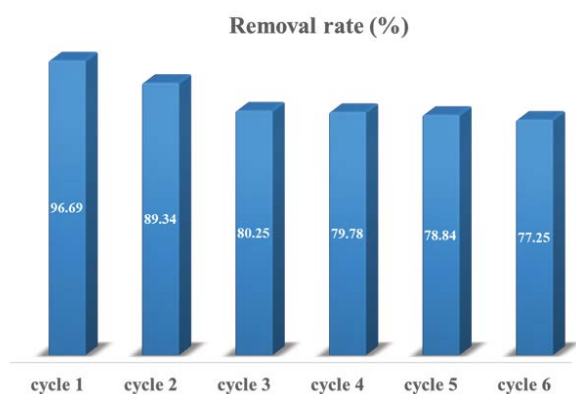


Fig. 14. Regeneration cycles of PCMW.

- [4] M. Massoudinejad, M. Ghaderpoori, A. Jafari, J. Nasehifar, A. Malekzadeh, A. Ghaderpoury, Data on nitrate and nitrate of Taham dam in Zanjan (Iran), *Data Brief*, 17 (2018) 431–437.
- [5] MEPPRC, Ministry of Environmental Protection of the People's Republic of China (MEPPRC), C.E.S. Bulletin, Ed., Beijing, 2018 (in Chinese).
- [6] L. Dong, L. Lin, Q. Li, Z. Huang, X. Tang, M. Wu, C. Li, X. Cao, M. Scholz, Enhanced nitrate-nitrogen removal by modified attapulgite-supported nanoscale zero-valent iron treating simulated groundwater, *J. Environ. Manage.*, 213 (2018) 151–158.
- [7] E.B. Baker, W.J. Showers, Hysteresis analysis of nitrate dynamics in the Neuse River, NC, *Sci. Total Environ.*, 652 (2018) 889–899.
- [8] M. Zhang, Y. Li, X. Long, Y. Chong, G. Yu, Z. He, An alternative approach for nitrate and arsenic removal from wastewater via a nitrate-dependent ferrous oxidation process, *J. Environ. Manage.*, 220 (2018) 246–252.
- [9] K. Hiller-Bittrolff, K. Foreman, A.N. Bulseco-McKim, J. Benoit, J.L. Bowen, Effects of mercury addition on microbial community composition and nitrate removal inside permeable reactive barriers, *Environ. Pollut.*, 242 (2018) 797–806.
- [10] S. Beganskas, G. Gorski, T. Weathers, A.T. Fisher, C. Schmidt, C. Saltikov, K. Redford, B. Stoneburner, R. Harmon, W. Weir, A horizontal permeable reactive barrier stimulates nitrate removal and shifts microbial ecology during rapid infiltration for managed recharge, *Water Res.*, 144 (2018) 274–284.
- [11] H.I. Uzun, E. Debik, Economical approach to nitrate removal via membrane capacitive deionization, *Sep. Purif. Technol.*, 209 (2019) 776–781.
- [12] Q. Gao, C.-Z. Wang, S. Liu, D. Hanigan, S.-T. Liu, H.-Z. Zhao, Ultrafiltration membrane microreactor (MMR) for simultaneous removal of nitrate and phosphate from water, *Chem. Eng. J.*, 355 (2019) 238–246.
- [13] X. Zhou, X. Zhang, Z. Zhang, Y. Liu, Full nitrification-denitrification versus partial nitrification-denitrification-anammox for treating high-strength ammonium-rich organic wastewater, *Bioresour. Technol.*, 261 (2018) 379–384.
- [14] Y. Huang, X. Chen, P. Li, G. Chen, L. Peng, L. Pan, Pressurized microcystis can help to remove nitrate from eutrophic water, *Bioresour. Technol.*, 248 (2018) 140–145.
- [15] X. Lei, F. Liu, M. Li, X. Ma, X. Wang, H. Zhang, Fabrication and characterization of a Cu-Pd-TNPs polycrystalline nanoelectrode for electrochemically removing nitrate from groundwater, *Chemosphere*, 212 (2018) 237–244.
- [16] J. El Mastour, S.E. El Qouatli, A. Chtaini, Electrochemical chelation and reduction of nitrate ion on EDTA modified carbon paste electrode, *Sens. Bio-Sens. Res.*, 21 (2018) 17–21.
- [17] J. Markovski, J. Garcia, K.D. Hristovski, P. Westerhoff, Nano-enabling of strong-base ion-exchange media via a room-temperature aluminum (hydr)oxide synthesis method to simultaneously remove nitrate and fluoride, *Sci. Total Environ.*, 599–600 (2017) 1848–1855.
- [18] A. Wei, J. Ma, J. Chen, Y. Zhang, J. Song, X. Yu, Enhanced nitrate removal and high selectivity towards dinitrogen for groundwater remediation using biochar-supported nano zero-valent iron, *Chem. Eng. J.*, 353 (2018) 595–605.
- [19] M. Kalaruban, P. Loganathan, J. Kandasamy, R. Naidu, S. Vigneswaran, Enhanced removal of nitrate in an integrated electrochemical-adsorption system, *Sep. Purif. Technol.*, 189 (2017) 260–266.
- [20] M. Niu, W. Xu, S. Zhu, Y. Liang, Z. Cui, X. Yang, A. Inoue, Synthesis of nanoporous CuO/TiO₂/Pd-NiO composite catalysts by chemical dealloying and their performance for methanol and ethanol electro-oxidation, *J. Power Sources*, 362 (2017) 10–19.
- [21] E. Sahinkaya, A. Yurtsever, D. Ucar, A novel elemental sulfur-based mixotrophic denitrifying membrane bioreactor for simultaneous Cr(VI) and nitrate reduction, *J. Hazard. Mater.*, 324 (2017) 15–21.
- [22] D. Ceconet, S. Zou, A.G. Capodaglio, Z. He, Evaluation of energy consumption of treating nitrate-contaminated groundwater by bioelectrochemical systems, *Sci. Total Environ.*, 636 (2018) 881–890.
- [23] R. Li, C. Feng, B. Xi, N. Chen, Y. Jiang, Y. Zhao, M. Li, Q. Dang, B. Zhao, Nitrate removal efficiency of a mixotrophic denitrification wall for nitrate-polluted groundwater in situ remediation, *Ecol. Eng.*, 106 (2017) 523–531.
- [24] P. Chris Wilson, J.P. Albano, Novel flow-through bioremediation system for removing nitrate from nursery discharge water, *J. Environ. Manage.*, 130 (2013) 192–198.
- [25] M. Kalaruban, P. Loganathan, W.G. Shim, J. Kandasamy, G. Naidu, T.V. Nguyen, S. Vigneswaran, Removing nitrate from water using iron-modified Dowex 21K XLT ion exchange resin: batch and fluidised-bed adsorption studies, *Sep. Purif. Technol.*, 158 (2016) 62–70.
- [26] L. Ao, F. Xia, Y. Ren, J. Xu, D. Shi, S. Zhang, L. Gu, Q. He, Enhanced nitrate removal by micro-electrolysis using Fe⁰ and surfactant modified activated carbon, *Chem. Eng. J.*, 357 (2019) 180–187.
- [27] Y. He, H. Lin, Y. Dong, B. Li, L. Wang, S. Chu, M. Luo, J. Liu, Zeolite supported Fe/Ni bimetallic nanoparticles for simultaneous removal of nitrate and phosphate: synergistic effect and mechanism, *Chem. Eng. J.*, 347 (2018) 669–681.
- [28] P. Kuang, N. Chen, C. Feng, M. Li, S. Dong, L. Lv, J. Zhang, Z. Hu, Y. Deng, Construction and optimization of an iron particle-zeolite packing electrochemical-adsorption system for the simultaneous removal of nitrate and by-products, *J. Taiwan Inst. Chem. Eng.*, 86 (2018) 101–112.
- [29] L. Zhao, H. Dong, R.E. Edelman, Q. Zeng, A. Agrawal, Coupling of Fe(II) oxidation in illite with nitrate reduction and its role in clay mineral transformation, *Geochim. Cosmochim. Acta*, 200 (2017) 353–366.
- [30] S. Cosnier, S. Da Silva, D. Shan, K. Gorgy, Electrochemical nitrate biosensor based on poly(pyrrole-viologen) film-nitrate reductase-clay composite, *Bioelectrochemistry*, 74 (2008) 47–51.
- [31] E.K. Saeidabadi, T. Ebadzadeh, E. Salahi, Preparation of mullite from alumina/aluminum nitrate and kaolin clay through spark plasma sintering process, *Ceram. Int.*, 44 (2018) 21053–21066.
- [32] Z. Keshavarz, D. Mostofinejad, Porcelain and red ceramic wastes used as replacements for coarse aggregate in concrete, *Constr. Build. Mater.*, 195 (2019) 218–230.
- [33] A. Turner, Lead pollution of coastal sediments by ceramic waste, *Mar. Pollut. Bull.*, 138 (2019) 171–176.
- [34] M.S. Khan, M. Sohail, N.S. Khattak, M. Sayed, Industrial ceramic waste in Pakistan, valuable material for possible applications, *J. Cleaner Prod.*, 139 (2016) 1520–1528.
- [35] L.S. Čerović, S.K. Milonjić, M.B. Todorović, M.I. Trtanj, Y.S. Pogožhev, Y. Blagoveschenskii, E.A. Levashov, Point of zero charge of different carbides, *Colloids Surf., A*, 297 (2007) 1–6.
- [36] M.P. Langeroudi, E. Binaeian, Tannin-APTES modified Fe₃O₄ nanoparticles as a carrier of methotrexate drug: kinetic, isotherm and thermodynamic studies, *Mater. Chem. Phys.*, 218 (2018) 210–217.
- [37] A. Alshameri, H. He, J. Zhu, Y. Xi, R. Zhu, L. Ma, Q. Tao, Adsorption of ammonium by different natural clay minerals: characterization, kinetics and adsorption isotherms, *Appl. Clay Sci.*, 159 (2018) 83–93.
- [38] A. Meghdadi, Characterizing the capacity of hyporheic sediments to attenuate groundwater nitrate loads by adsorption, *Water Res.*, 140 (2018) 364–376.
- [39] A. Derylo-Marczewska, M. Blachnio, A.W. Marczewski, M. Seczkowska, B. Tarasiuk, Phenoxyacid pesticide adsorption on activated carbon – equilibrium and kinetics, *Chemosphere*, 214 (2019) 349–360.
- [40] K. Jafari, M. Heidari, O. Rahmadian, Wastewater treatment for amoxicillin removal using magnetic adsorbent synthesized by ultrasound process, *Ultrason. Sonochem.*, 45 (2018) 248–256.
- [41] C.H.C. Tan, S. Sabar, M.H. Hussin, Development of immobilized microcrystalline cellulose as an effective adsorbent for methylene blue dye removal, *South Afr. J. Chem. Eng.*, 26 (2018) 11–24.
- [42] I. Gulgonul, M.S. Çelik, Understanding the flotation separation of Na and K feldspars in the presence of KCl through ion exchange and ion adsorption, *Miner. Eng.*, 129 (2018) 41–46.
- [43] C.-H. Zhou, D. Zhang, D.-S. Tong, L.-M. Wu, W.-H. Yu, S. Ismajli, Paper-like composites of cellulose acetate-organomontmorillonite for removal of hazardous anionic dye in water, *Chem. Eng. J.*, 209 (2012) 223–234.

- [44] Z. Harrache, M. Abbas, T. Aksil, M. Trari, Thermodynamic and kinetics studies on adsorption of Indigo Carmine from aqueous solution by activated carbon, *Microchem. J.*, 144 (2019) 180–189.
- [45] H.M. Jang, S. Yoo, Y.-K. Choi, S. Park, E. Kan, Adsorption isotherm, kinetic modeling and mechanism of tetracycline on *Pinus taeda*-derived activated biochar, *Bioresour. Technol.*, 259 (2018) 24–31.
- [46] S. Jellali, M.A. Wahab, M. Anane, K. Riahi, N. Jedidi, Biosorption characteristics of ammonium from aqueous solutions onto *Posidonia oceanica* (L.) fibers, *Desalination*, 270 (2011) 40–49.
- [47] X. Song, X. Lü, Y. Shen, S. Guo, Y. Guan, A modified supercritical Dubinin–Radushkevich model for the accurate estimation of high pressure methane adsorption on shales, *Int. J. Coal Geol.*, 193 (2018) 1–15.
- [48] W. Hamza, N. Dammak, H.B. Hadjltaief, M. Eloussaief, M. Benzina, Sono-assisted adsorption of crystal violet dye onto Tunisian Smectite clay: characterization, kinetics and adsorption isotherms, *Ecotoxicol. Environ. Saf.*, 163 (2018) 365–371.
- [49] R. Nitzsche, A. Gröngroft, M. Kraume, Separation of lignin from beech wood hydrolysate using polymeric resins and zeolites – determination and application of adsorption isotherms, *Sep. Purif. Technol.*, 209 (2019) 491–502.
- [50] S. Jain, A. Bansiwala, R.B. Biniwale, S. Milmlle, S. Das, S. Tiwari, P. Siluvai Antony, Enhancing adsorption of nitrate using metal impregnated alumina, *J. Environ. Chem. Eng.*, 3 (2015) 2342–2349.
- [51] Y. Wan, X. Liu, P. Liu, L. Zhao, W. Zou, Optimization adsorption of norfloxacin onto polydopamine microspheres from aqueous solution: kinetic, equilibrium and adsorption mechanism studies, *Sci. Total Environ.*, 639 (2018) 428–437.
- [52] A. Vahdat, B. Ghasemi, M. Yousefpour, Synthesis of hydroxyapatite and hydroxyapatite/Fe₃O₄ nanocomposite for removal of heavy metals, *Environ. Nanotechnol. Monit. Manage.*, 12 (2019), doi: 10.1016/j.enmm.2019.100233.
- [53] B.C. Erdoğan, S. Ülkü, Ammonium sorption by Gördes clinoptilolite rich mineral specimen, *Appl. Clay Sci.*, 54 (2011) 217–225.
- [54] H. Javadian, B.B. Koutenaee, E. Shekarian, F.Z. Sorkhrodi, R. Khatti, M. Toosi, Application of functionalized nano HMS type mesoporous silica with N-(2-aminoethyl)-3-aminopropyl methylmethoxysilane as a suitable adsorbent for removal of Pb(II) from aqueous media and industrial wastewater, *J. Saudi Chem. Soc.*, 21 (2017) S219–S230.
- [55] E. Carazo, A. Borrego-Sánchez, R. Sánchez-Espejo, F. García-Villén, P. Cerezo, C. Aguzzi, C. Viseras, Kinetic and thermodynamic assessment on isoniazid/montmorillonite adsorption, *Appl. Clay Sci.*, 165 (2018) 82–90.
- [56] Y. Liu, D. Ying, L. Sanguansri, Y. Cai, X. Le, Adsorption of catechin onto cellulose and its mechanism study: kinetic models, characterization and molecular simulation, *Food Res. Int.*, 112 (2018) 225–232.
- [57] M. Kumar, H.S. Dosanjh, H. Singh, Biopolymer modified transition metal spinel ferrites for removal of fluoride ions from water, *Environ. Nanotechnol. Monit. Manage.*, 12 (2019), doi: 10.1016/j.enmm.2019.100237.
- [58] J. Yang, H. Li, D. Zhang, M. Wu, B. Pan, Limited role of biochars in nitrogen fixation through nitrate adsorption, *Sci. Total Environ.*, 592 (2017) 758–765.
- [59] N. Öztürk, T.E.L. Bektaş, Nitrate removal from aqueous solution by adsorption onto various materials, *J. Hazard. Mater.*, 112 (2004) 155–162.
- [60] C. Fan, Y. Zhang, Adsorption isotherms, kinetics and thermodynamics of nitrate and phosphate in binary systems on a novel adsorbent derived from corn stalks, *J. Geochem. Explor.*, 188 (2018) 95–100.